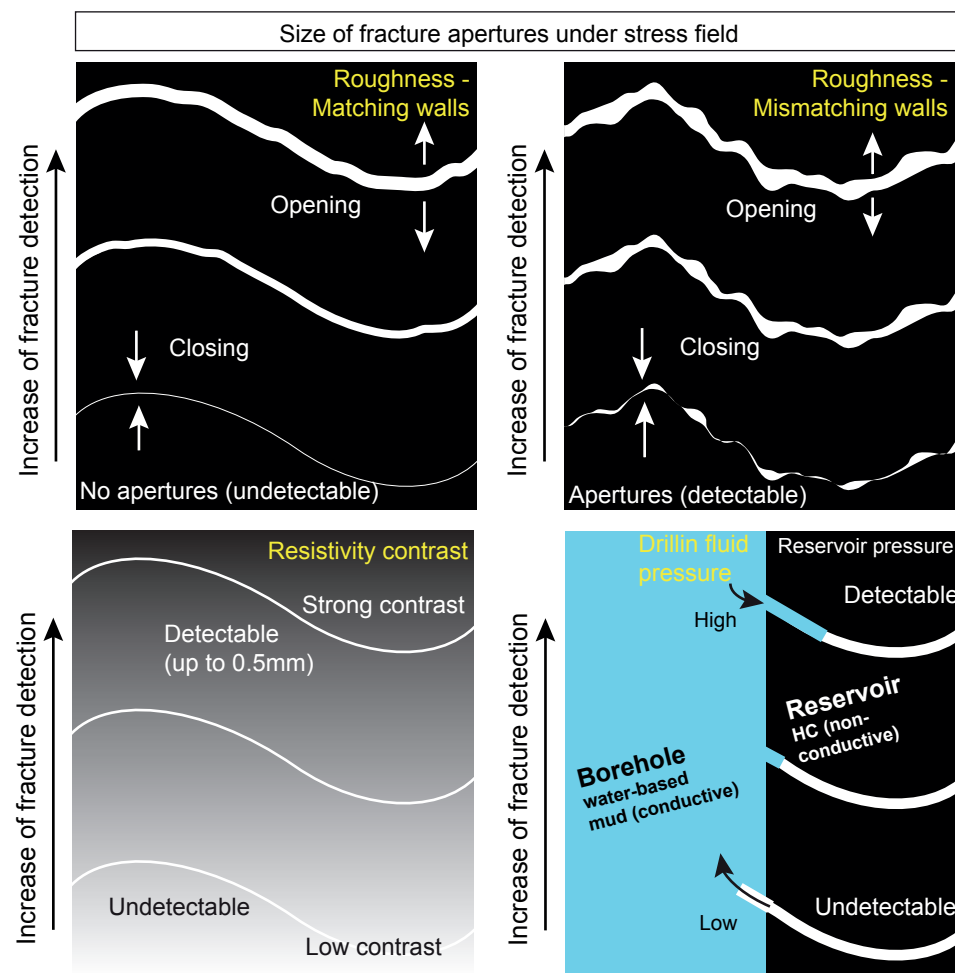


Factors influencing detections of subsurface fractures using electrical borehole images



1 **Comparison of carbonate reservoir fractures from core and modern**
2 **electrical borehole images**
3
4 3 *M. M. Al-Fahmi^{1,2 *} and Joe A. Cartwright¹*
5
6 4 1. *University of Oxford, Oxford, UK*
7
8 5 2. *Saudi Aramco, Dhahran, Saudi Arabia*
9
10 6 * *Corresponding author: alfahmi@gmail.com*
11
12
13

14 7 **Abstract**
15

16
17 8 Several methods exist for collecting data about opening-mode fractures
18
19 9 (hereinafter fractures) in subsurface reservoir rocks. The datasets, with the
20
21 10 exception of core data, are indirect and subject to limited resolutions. This
22
23 11 paper includes new results on the detection of fractures in carbonate
24
25 12 reservoirs by modern electrical borehole imagers. Barren fractures and
26
27 13 calcite-filled fractures (calcite veins) were described and compared from
28
29 14 whole core and borehole images. These datasets were obtained from
30
31 15 directional drilling into the Arab petroleum reservoirs in a low-relief dome
32
33 16 structure in Eastern Arabia. The comparison of fracture abundance resulted in
34
35 17 a significant mismatch, because many reservoir fractures in the core could not
36
37 18 be detected from corresponding borehole images. Most calcite veins were
38
39 19 undetected because of their small widths, below 2 mm. Exceptions include a
40
41 20 few calcite veins of 0.5 mm that were detected because of the strong contrast
42
43 21 between resistive veins and conductive host rock beds. The barren fractures
44
45 22 that are aligned sub-parallel to the maximum horizontal principal stress
46
47 23 (S_{Hmax}) were detected more abundantly than other non-aligned barren
48
49 24 fractures. The present-day S_{Hmax} is roughly trending between 60° to 100°
50
51 25 azimuth in Eastern Arabia. The aligned fractures have larger apertures in the
52
53
54
55
56
57
58
59
60
61
62
63
64
65

borehole images than the non-aligned fractures. Consistent with this finding was another important finding: Aligned fractures exhibit relatively large apertures in the borehole images. The apertures diminish in size as the fractures gradually deviate in orientation from the S_{Hmax} . Most of the non-aligned barren fractures were undetected, except the fractures with rough and mismatching walls. This indicates that the walls of the non-aligned fractures are mechanically closed by the normal S_{Hmax} , and that the remaining apertures were dependent on the availability of roughness mismatches between the closed fracture walls. Electrical borehole images are biased in measuring fracture abundance, but indispensable to detect and measure the orientations and apertures of fractures, especially the large (i.e., more conductive) fractures in reservoir rocks.

1. Introduction

Fractures are key parameters influencing the hydraulic and mechanical properties of rock masses, depending on the properties and abundance of fractures. Diverse methods exist in the petroleum industry for describing some fracture properties in reservoir rocks, but the datasets underpinning this effort are predominantly indirect and subject to limitations of data resolution, sampling dimensions and calibrations (e.g., Nelson, 2001). Whole core and borehole images provide the best data to observe fractures and describe fracture properties along boreholes. But because coring is either expensive to acquire, non-oriented, or of poor quality for fracture characterization, borehole images are commonly used to describe fracture abundance, apertures and

1
2
3
4
5
6
7
8
9
10
11
12
13
14
15
16
17
18
19
20
21
22
23
24
25
26
27
28
29
30
31
32
33
34
35
36
37
38
39
40
41
42
43
44
45
46
47
48
49 orientations in subsurface reservoir rocks (e.g., Luthi and Souhaité, 1990;
50 Ozkaya, 2008; Ameen et al., 2010; Ogata et al., 2014).

51 Numerous studies have described fractures from borehole images, but
52 relatively a few studies from the petroleum industry and the scientific drilling
53 programs have directly compared fractures from core with their corresponding
54 interval on an electrical borehole image, see review in (Al-Fahmi, 2018). The
55 studies have provided important perspectives on the electrical borehole
56 imaging of fractures in different reservoir and non-reservoir rocks.
57 Nevertheless, the results were often limited by (i) the low core recovery from
58 fractured intervals, (ii) the restricted extent of borehole coverage and
59 resolution of old imaging tools, and (ii) the use of vertical boreholes, which
60 miss vertical and subvertical fracture sets (Al-Fahmi, 2018).

61 The electrical borehole imagers have been improved since their early
62 development in the 1980s (Ekstrom et al., 1986). For example, the Formation
63 Microlmager (FMI) can provide a better coverage and resolution of borehole
64 walls than its predecessor; the Formation MicroScanner (FMS), see (e.g.,
65 Pöppelreiter et al., 2010; Brown et al., 2013).

66 In this paper, we address borehole imaging of carbonate reservoir fractures
67 from an unusually comprehensive database of core and FMI borehole images
68 (Table 1). The core was obtained with an excellent (98%) recovery, and the
69 borehole images are of excellent resolution and coverage of the borehole
70 walls. The datasets were obtained during an extended reach drilling campaign
71 from four boreholes (X-01, X02, X-03 and X-04) (Fig. 1.b, c). The boreholes
72 were drilled into the Arab carbonate reservoirs in a dome structure in Eastern
73 Arabia (Fig. 1 and Table 1). This is an area where the regional stress field is

well documented (e.g., Ameen, 2014) (Fig. 1a). The orientations of X-01 and X-02 are almost parallel to the regional trend of the S_{Hmax} , and the X-03 and X-04 are oblique to the S_{Hmax} (Fig. 1a, b). The drilling and coring were done by the same operator and the same service company during a short period of time in 2013. The aims of this paper are to: 1) report abundance of fractures from whole core and corresponding intervals of borehole images, and 2) explain the factors that reduce or enhance detection of fractures by electrical borehole imaging. Given that the electrical borehole imaging is an evolving technology that is cheaper than coring, it is important and timely to shed lights on how the fracture data from modern tools directly compares with what is observed from an equivalent core.

2. Geologic background

The study area is part of an onshore petroleum field of a low-relief dome, occupying about 110 square kilometers in Eastern Arabia (Al-Fahmi et al., 2016, 2014), (Fig. 1a, b). The dome is among many dome structures in the eastern regions of the Arabian Platform that evolved by the growth of deeply buried, non-piercing pillows of the Hormuz Salt (e.g., Al-Fahmi et al., 2016). The development of domes and anticlines in the Arabian Platform was a major mechanism for trapping oil and gas in the major carbonate reservoirs of the Late Permian Khuff and the Late Jurassic Hanifa and Arab rock formations. This research is on the fractures in the Arab carbonate reservoirs, which are approximately located at about 1400-m depth below ground level in the study area (Fig. 1a). The carbonate members (A, B, C, D) of the Arab Formation are composed of a variety of skeletal grainstones, packstones and

ooid grainstones (e.g., Mitchell et al., 1988) (Fig. 2). The carbonates are known for high porosity and permeability intervals, which make the Arab-D in particular the world's most prolific and producing petroleum-bearing rock.

Many publications (e.g. Ameen et al., 2010; Ameen, 2014; MacPherson and Ameen, 2014) and unpublished Aramco reports indicate based on results from borehole imaging that barren, conductive (open) fractures in the Arab, Hanifa and Khuff reservoirs exist in two major systems: A dominant east-west (E-W) to northeast-southwest (NE-SW) system, and a subordinate northwest-southeast (NW-SE) system; refer to the region defined by Ameen et al. (2010) as Domain B. The NE-SW and E-W fracture systems are aligned or closely aligned parallel with the present-day S_{Hmax} , which trends between 60° to 100° in Eastern Arabia (Fig. 1a). The S_{Hmax} is higher than the vertical stress (S_v) of sediment load and is linked to the Zagros compressional field induced by the collision of the Arabian/Eurasian Plates (e.g., Ameen et al., 2010).

3. Datasets

The core is 91.4 m with 6-cm diameter from X-01 and 189 m with 8-cm diameter from X-03 (Fig. 1 and Table 1). Core operations resulted in 98% recovery, with no more than 4.57 m damaged from the 283.5 m cored intervals. The core was mostly in its solid and whole cylindrical shape (Fig. 3a, b).

The borehole images were acquired from the four boreholes using modern electrical borehole imagers that are described in Brown et al. (2013). The boreholes were drilled with a water-based mud system, which is ideal for the

121 two types of the used imaging tools; wireline imagers (FMI HD) in the cored
122 boreholes X-01 and X-03, and Logging While Drilling (LWD) borehole imager
123 (FMI MicroScope HD) in X-02 and X-04 (Table 1). The borehole images of X-
124 01, X-03, and X-04 were acquired under similar borehole conditions of mud
125 pressure. The borehole images of X-02 were acquired while drilling with a
126 mud pressure higher than the reservoir fluid pressure. Consequently, the mud
127 was partially lost in the Arab reservoirs.

128 The caliper data from the four boreholes display cylindrical smooth boreholes,
129 ideal for obtaining good images. The wireline images are excellent throughout
130 the carbonate reservoirs, showing details of rock fabrics such as sharp
131 bedding contacts, fractures, and rock pores of up to 1mm. The images of the
132 X-02 and X-04 boreholes are excellent from this newly developed LWD tool,
133 see (e.g., Amer et al., 2013; Wang and Thagafy, 2017). According Wang and
134 Thagafy (2017), these LWD tools have similar resolution of geological
135 features such as bedding planes, fractures and borehole breakouts. The LWD
136 images, however, appear pixilated and occasionally blurry when compared to
137 the wireline images, and hence seem to provide fewer details about rock
138 fabrics and fractures.

139 **4. Methodology**

140 *4.1. Dataset preparation*

141 The close-fitting core was scanned using an industrial scanner, which
142 produced 360° photographs of core exterior in true color with a resolution of
143 up to 10 pixel/mm, and details up to 40 pixel/mm (Fig. 3b). In addition, the
144 spectral gamma ray was measured from the core and used to tie its depths to
145 that of the borehole logs including the borehole images. Later, the core was

146 slabbed and the thin sections were sampled for routine lithological
147 descriptions (Fig. 3c). Raw data from the borehole imaging tools were
148 processed using Techlog, an industrial software application. The methods of
149 processing borehole images are commonplace in the petroleum industry (e.g.,
150 Brown et al., 2013).

151 4.2. Interpretation

152 The core and borehole images were interpreted for stratigraphical and
153 structural features such as fractures, bedding planes, and drilling-induced
154 fractures (DIFs). Furthermore, the core was described for lithofacies from
155 slabbed core and thin sections, following a modified version of Dunham
156 classification (Dunham, 1962) (Fig. 2).

157 Fractures were categorized into barren fractures and mineral-filled fractures
158 (veins) from the core and borehole images. The veins include any fracture
159 whose walls are bonded or bridged with minerals, or separated but coated by
160 mineral crystals that are distinguishable from the host rock minerals.
161 Otherwise, the fractures were categorized as barren fractures. Barren
162 fractures were interpreted from the core on the basis of consistent dips and
163 strikes (parallel sets), oil stain, surface morphology, and trace shape (Al-
164 Fahmi, 2018). Many fractures were matched from both core and borehole
165 images in location, steep dips, and planar shapes. Other fractures were
166 interpreted based on criteria above, although were missing from the borehole
167 images (Al-Fahmi, 2018). The barren fracture interpretation was facilitated by
168 the borehole orientations, which are neither perpendicular to bedding nor to
169 the planes of steeply dipping fractures. It is important to note here that the

170 detection of barren open fractures in borehole images depend on the
171 infiltration of the conductive drilling fluids into fractures (e.g., Spies, 1996).
172 The fracture detection in borehole images is reduced if fractures are of low-
173 data (resistivity/conductivity) contrast against their host rocks (Ponziani et al.,
174 2015). The data contrast may be improved by image processing techniques
175 (Ekstrom et al., 1987), however, the processing techniques cannot help
176 distinguish the fractures from the host rocks if their electrical properties are
177 similar or moderated by the drilling fluid types (e.g., Tehrani et al., 2002;
178 Khoshbakht et al., 2012).

179 The interpreted fractures and veins from the core were profiled and digitized
180 from the 360° photographs of core exterior (Fig. 4). The digital profiles were
181 used to measure width, roughness, and wall mismatch. Fractures with edges
182 displaying signs of an artificial damage were excluded from the
183 measurements of fracture width, roughness, and wall mismatch (Fig. 4b).

184 **5. Fracture characterization**

185 The fractures and veins were characterized for orientation, width, roughness,
186 wall mismatch, and abundance from the datasets whenever possible. The
187 fracture properties are briefly defined here, and further details are described
188 by Al-Fahmi (2018).

189 *5.1. Orientation*

190 Fracture orientation is often defined by dips and strikes. The orientations of
191 fractures and veins were measured from the borehole images. The core was

not oriented to measure fracture strikes, but the fracture dips were measurable against the host bed dips.

5.2. Fracture width

Fracture width in the core was measured for the arithmetic mean of the physical (mechanical) separation between fracture walls, regardless if the fracture was void or filled by minerals. Hence, fracture width defines the thickness of veins and the mechanical aperture of barren fractures in the core. Sections of maximum and minimum widths along the profiles were measured and averaged using a digital scale comparator, (Fig. 4c).

Fracture apertures were measured from the borehole images of X-01 and X-03 using the methods described in Luthi and Souhaité (1990). The methods are available in the industrial software applications commonly used for the FMI image processing and interpretation. The fracture mechanical aperture (W) was measured by this relationship:

$$W = cAR_m^b R_{xo}^{1-b} \quad (1)$$

as a function of the integrated additional mud current A , the resistivity of the formation R_{xo} , and the resistivity of the mud R_m , through the FMI-tool-dependent coefficients b and c (Luthi and Souhaité, 1990). The mean mechanical aperture was measured by this relationship:

$$W_m = \frac{\sum W^3 n}{n} \quad (2)$$

212 as the sum of mechanical apertures (from sampled points) along the fracture
213 trace averaged over fracture length in the borehole (e.g., Luthi and Souhaité,
214 1990). The mean hydraulic aperture was measured by this relationship:

$$W_h = \sqrt[3]{\frac{\sum W^3_n}{n}} \quad (3)$$

216 as the cubic mean of the mean of the cubes of mechanical aperture (W). This
217 latter relationship was provided by the imaging tool manufacturer based on
218 calibrations to production data. In the relationship, the hydraulic aperture of a
219 fracture is equal, or greater than the mechanical aperture if fracture walls are
220 not perfectly parallel (i.e., of mismatching walls). It is important to note that
221 this relationship (3) differs from the conventional rock mechanical methods, in
222 which hydraulic aperture is either equal, or smaller than the mechanical
223 aperture if fracture walls are mismatching (e.g., Barton et al., 1985).

224 5.3. *Roughness and wall mismatch*

225 Roughness refers to the fracture wall undulations, which can be estimated
226 using the joint roughness coefficient (JRC) (e.g., Barton and Choubey, 1977).
227 The JRC is scale of ten typical profiles ranging from very smooth (0-2 profile)
228 to very rough (18-20 profile) (e.g., Barton and Choubey, 1977). Wall mismatch
229 refers to the deviation of fracture walls from parallel (i.e., matching) walls
230 (e.g., Zhao, 1997). It can be estimated using a wall mismatching coefficient
231 (WMC) by quantitatively correlating roughness of the two fracture walls (Al-
232 Fahmi et al., 2018). The WMC ranges between 0 to 1; the 0 value indicates
233 perfectly matching fracture walls (Al-Fahmi et al., 2018). The JRC and WMC
234 were measured from the separated top and base traces of fracture profiles

1
2
3
4
5
6
7
8
9
10
11
12
13
14
15
16
17
18
19
20
21
22
23
24
25
26
27
28
29
30
31
32
33
34
35
36
37
38
39
40
41
42
43
44
45
46
47
48
49
50
51
52
53
54
55
56
57
58
59
60
61
62
63
64
65

235 using several computational methods, which were described in a separate
236 publication (Al-Fahmi et al., 2018) (Fig. 4d).

237 5.4. *Fracture abundance*

238 Fracture abundance refers to the number of fractures per distance (e.g.,
239 Dershowitz and Herda, 1992). Fracture abundance was measured along the
240 borehole sections, from the core and borehole images. Comparisons of
241 fracture abundance were made on the core intervals C1, C2, and C3 of X-01,
242 and from the core intervals C5, C6, C7, and C8 of X-03, (Fig. 1c). There were
243 no borehole images of the borehole equivalent to the upper 6.7 m of C5 and
244 entire C4 of X-01. The core circumference and the images of the equivalent
245 borehole walls are equal sections for the probability of fracture intersections.
246 The volume gap, about 6-cm separation between the core and borehole wall,
247 does not impair the comparison of sub-vertical fractures described from
248 deviated cores. The intervals of missing core and the fractured core samples
249 that could not be interpreted were excluded from the fracture abundance
250 comparisons.

251 **6. Results**

252 The descriptions of fracture properties from the core and borehole images are
253 included in (Al-Fahmi, 2018). The main observations are summarized in the
254 following subsections.

255 6.1. *Fracture properties*

- 1) Fractures in the core and borehole images occur in two types: barren fractures and calcite veins (Fig. 5).
- 2) The barren fractures and calcite veins are of steep dips to the nearly flat bedding strata of the Arab reservoirs, (Fig. 5) and (Fig. 6a, c, d). Majority of the calcite veins exhibit strikes of NW-SE to E-W azimuth (Fig. 6d). The strikes of barren fractures exhibit a wide azimuth range that can be roughly divided into NW-SE, E-W and NE-SW azimuths (Fig. 6c). The histograms of individual boreholes in Fig. 6b show a narrow range of fracture strikes of nearly normal azimuth to the borehole trajectories. The NE-SW and E-W fractures were greatly missed by the X-1 and X-02 boreholes, but were intersected in the study area by X-03 and X-04 boreholes (Fig. 6b).
- 3) Calcite veins in the core exhibit widths mostly below 2 mm (Fig. 7.a). Barren fractures exhibit apertures mostly below 5 mm in the core, and below 1 mm in borehole images (Fig. 7a). The aperture measurements of the detected barren fractures in the borehole images display parallel trends from X-01 and X-03, with mean apertures increasing toward the fractures striking E-W and NE-SW ($\sim 60\text{-}100^\circ$), and decreasing toward the fractures striking NW-SE ($\sim 120\text{-}180^\circ$), (Fig. 7b). Measured apertures from the borehole images (Fig. 7b) display a difference (i.e., curve separation) between the mechanical apertures and hydraulic apertures. In addition, the detected individual apertures exhibit more variations and small sizes in X-01 than in X-03.
- 4) Rough and wall-mismatching fractures in the core display generally larger sizes than smooth and wall-matching fractures (Fig. 7c). Rough

and wall-mismatching fractures tend to be detected in the corresponding borehole images more frequently than the smooth and wall-matching fractures (Fig. 7a, d). Most of the barren fractures were found to be wall matching, but a minority of the fractures have noticeable wall mismatch (Al-Fahmi et al., 2018). Furthermore, roughness and wall mismatches were found to be product of the lithological facies (sizes and shapes of grains, crystals and pores) of the host limestones and dolomites (Al-Fahmi et al., 2018).

6.2. Abundance of fractures and veins

- 1) About 80% of the interpreted fractures are barren fractures and the remaining are calcite veins (Fig. 8).
- 2) The number of barren fractures and calcite veins described from the core considerably outnumbers those interpreted from corresponding borehole images (Fig. 8). Calcite veins are particularly less pronounced from the borehole images. The borehole images are inconsistent for measuring the abundance of fractures and veins: the detection levels vary and range from 0% to 100% of what was observed and counted from the corresponding core (Fig. 8).
- 3) The borehole images of X-03 had significantly better detection level for the barren fractures than the borehole images of X-01 (Fig. 8). The barren fractures that were missed by the borehole images account for 83% from X-01 and 45% from X-03 (Fig. 8).
- 4) Some exceptional observations were also noted during the comparisons of fractures and veins. A core barren fracture of a

relatively large width of 5 mm was difficult to detect in the borehole image. The vuggy nature of the host rock masks the fracture, which has a “rough” texture similar in rugosity to the vugs, (Fig. 9a). In addition, a few calcite veins of 0.5-mm widths were detected from the borehole images, (Fig. 9b). These calcite veins were located in a porous limestone interval. The signatures of fracture apertures varied in the borehole images, from those of partial traces to those of complete and large apertures. The fractures of outstanding large apertures were especially noted from the LWD images of X-02, see (Fig. 10) for comparisons.

7. Discussion

The comparisons in Fig 8 display that borehole images provide reduced and inconsistent detections for abundance of reservoir fractures and veins. This is mostly related to the size of fracture widths, imaging resolutions, and resistivity contrast between fractures and host rock. There is, however, an obvious interplay between the size of barren fracture apertures, and other factors including fracture roughness and the behavior of barren fractures under the tectonic compressive stress (namely, the present-day S_{Hmax} in Eastern Arabia). These factors are discussed below.

7.1. Fracture width

The majority of calcite veins were not identifiable in the borehole images because the calcite veins exhibit widths below 2 mm. Nevertheless, some calcite veins of 0.5 mm were detected, but apparently because of the high

data contrast between these resistive fractures and their conductive host rocks. This is consistent with previous reports that rock features with a high resistivity contrast can be detected in borehole images even if they are smaller than the imaging sampling intervals (e.g., Brown et al., 2013). The widths of calcite veins are finite, and can accordingly indicate the borehole imaging quality. The barren fractures with larger mean apertures exhibit a higher probability to be visible from corresponding borehole images (Fig. 7a). Aperture sizes are obviously dynamic, changing according to the stress field. They may also change over time, while and after drilling and imaging the borehole. The aperture measurements in Fig. 7a are interpreted qualitatively, as they may not characterize the real apertures under the subsurface compression on fracture walls. It is because the core at surface is at a relaxed mechanical state. The range of aperture sizes from borehole images seems representative, although there is no independent method to confirm if these apertures are exact in the subsurface reservoirs. The apertures seem small, but recent lab experiments (Ponziani et al., 2015) validated measuring such small apertures below 1 mm. Nonetheless, the detected barren fractures must have apertures for infiltrating drilling fluid that makes the fractures visible as highly conductive (complete or partial) traces in borehole images. In contrast, the undetected barren fractures must be mechanically closed, preventing infiltrations of drilling fluids into any part along the fractures.

7.2. *Present-day stress field*

The detection of barren fractures using borehole imaging depends on the size of fracture apertures, which are apparently sensitive to the SHmax in Eastern

Arabia). Fracture detection from the images of X-03 borehole was better than from the images of X-01 borehole (Fig. 8), because the X-03 borehole intersected some of the E-W and NE-SW (aligned) fractures (Fig. 6b). These aligned fractures exhibit larger apertures (Fig. 7b), and so were easily detected. The non-aligned fractures were mostly undetected as they are apparently closed under the SHmax. The results have implications on the descriptions of reservoir fractures in tectonically active regions such as Eastern Arabia. Firstly, the detectable apertures of the aligned fractures present a bias in the frequency of fractures. This bias indicates why the NE-SW fractures, interpreted from borehole images, make up the dominant system in the carbonate reservoirs in Eastern Arabia (e.g., Ameen et al., 2010; Ameen, 2014). Secondly, the bias of borehole images toward detecting fractures of large apertures is very useful to model the preferred paths of fluid flow in reservoir rocks (Heffer and Lean, 1993). The fractures can be modeled with gradual increase, or decrease, in aperture sizes according to the fracture orientations with respect to the active tectonic stress.

7.3. *Fracture roughness and wall mismatch*

The wall mismatch, especially of rough fractures, contributed to the fracture mean sizes (Fig. 7a, c), and therefore influenced the fracture detections. Wall-mismatching fractures are generally found with larger mean apertures than the wall-matching fractures (Fig. 7a). Furthermore, the measurements demonstrate a separation between the mechanical and hydraulic apertures, indicating wall mismatches in the detected barren open fractures (Fig. 7b). In a parallel study, Al-Fahmi et al. (2018) found out that most of the barren

fractures showing wall matching, but a minority (~24%) of them have noticeable wall mismatches (Fig. 7d). This is consistent with the detection of a small percentage of the NW-SE barren fractures, especially in the borehole images of X-01 (Fig.7b). The S_{Hmax} apparently reduced or closed apertures of the NW-SE fracture system, except where wall mismatches prevented complete contacts of fracture walls.

7.4. Resistivity of fractures and host rock

The water-based mud was optimal in this case study for the fracture detections. However, a few fractures were either unexpectedly undetected, or detected such as the calcite veins of 0.5-mm widths (Fig. 9). The factor of resistivity contrast was noted for a limited number of the detected fractures and veins. It is not possible, however, to specify if certain fractures were also missed because of the lack of resistivity contrast. Nonetheless, the conductive fractures and resistive calcite veins generally differ in their degrees of resistivity from those of the host carbonate rocks.

7.5. Drilling fluid pressure

The relatively large apertures of the fractures observed from the LWD images of X-2, Fig. 10, are interpreted to be the product of the drilling with high fluid pressure. The LWD images are inferior in quality to wireline images, so the observed large apertures in X-02 must have been increased greatly for electrical imaging by the conductive mud infiltrate. This observation of large apertures could not be related to the pixilation of the processed images, as there are other open fractures in the same LDW images with narrower

1
2
3
4
5
6
7
8
9
10
11
12
13
14
15
16
17
18
19
20
21
22
23
24
25
26
27
28
29
30
31
32
33
34
35
36
37
38
39
40
41
42
43
44
45
46
47
48
49
50
51
52
53
54
55
56
57
58
59
60
61
62
63
64
65

399 apertures matching the ones observed from the wireline images, (Fig. 10).
400 This is an exceptional case of the drilled boreholes, although provided
401 important insights on how the LWD images gave instant (LWD)
402 measurements for the behavior of barren fractures under high pressure of
403 drilling fluid infiltrations (Prilliman et al., 1997). This view remains qualitative,
404 in absence of quantitative techniques that can measure fracture apertures
405 from the LWD imaging tool data. It seems from this observation that borehole
406 imaging with over-balance drilling (i.e., with drilling-fluid pressure higher than
407 the reservoir fluid pressure such as the case of X-02) may improve signatures
408 and detection level for barren fractures. The ability of the conductive drilling
409 fluid to permeate through fractures, and locally displace the non-conductive
410 petroleum, may depend on the fluid equilibrium between the borehole
411 pressure and the reservoir pressure.

412 **8. Conclusions**

413 This paper demonstrated new results on the detection of carbonate fractures
414 by electrical borehole imagers (FMI HD). This study used high-quality
415 datasets, of core and borehole images, from boreholes optimally deviated to
416 intersect subvertical fractures in the Arab carbonate reservoirs. The reservoir
417 fractures, existing as barren fractures and calcite veins, were described and
418 directly compared between core and corresponding intervals of borehole
419 images. The comparison resulted in a significant mismatch in measuring
420 fracture abundance. The borehole imaging provides generally limited
421 detection of fractures, and hence significantly lower fracture abundance from
422 the reservoirs. Nevertheless, the borehole imaging provides important

information on measuring orientations and apertures of reservoir rock fractures. In general, fractures were detected by borehole imaging because they exhibit sizes greater than about 2 mm. The borehole imaging, however, detected much smaller fractures of 0.5mm finite widths. This is attributed to the contrast between the resistivity data of these fractures and the host rock intervals. Significantly, the borehole imaging revealed that the sizes of fracture apertures depend on the present-day stress field (S_{Hmax}) in Eastern Arabia. The results indicate that the barren fractures that are aligned with the S_{Hmax} are open. Their apertures are large enough to be easily detected by the borehole imaging. The non-aligned barren fractures are closed under the same stress field, except the fractures with remaining apertures preserved by rough-wall mismatches. The detected barren fractures are (partially or completely) open. The undetected fractures are completely closed for fluid flow. The imaging detection of barren fractures can further be influenced by drilling fluid pressure. Drilling with high-pressure fluids seem comparable to the stress field; opening mechanically closed fractures or increasing aperture sizes. The observations from this study are summarized and presented in Fig. 11. The study results have direct implications on the characterization of subsurface rock fractures. In particular, the biased borehole imaging results on fracture abundance lead to erroneous use of the fracture dominant trends as *paleo* stress trajectories in the structural and tectonic analyses of sedimentary basins. The same biased results toward detecting large and open fractures are rather very useful for modeling the preferred fluid flow directions in subsurface reservoir rocks.

Acknowledgments

1
2
3
4
5
6
7
8
9
10
11
12
13
14
15
16
17
18
19
20
21
22
23
24
25
26
27
28
29
30
31
32
33
34
35
36
37
38
39
40
41
42
43
44
45
46
47
48
49
50
51
52
53
54
55
56
57
58
59
60
61
62
63
64
65

448 We thank Saudi Aramco, especially the Reservoir Characterization
449 Department, for funding this project, and for giving us the data and permission
450 to publish this paper. This work is part of Al-Fahmi's PhD project at Oxford
451 University. Support from Oxford's Department of Earth Sciences is highly
452 appreciated.

453

454 References

- 455 Al-Fahmi, M.M., 2018. Controls on fracture abundance in gently deformed
456 carbonates, PhD thesis. University of Oxford.
- 457 Al-Fahmi, M.M., Cooke, M.L., Cole, J.C., 2014. Modeling of the Damman outcrop
458 fractures: Case study for fracture development in salt-cored structures.
459 GeoArabia, J. Middle East Pet. Geosci. 19, 49–80.
- 460 Al-Fahmi, M.M., Ozkaya, S.I., Cartwright, J.A., 2018. New insights on fracture
461 roughness and wall mismatch in carbonate reservoir rocks. Geosphere 14, 1851–
462 1859. doi:10.1130/GES01612.1
- 463 Al-Fahmi, M.M., Plesch, A., Shaw, J.H., Cole, J.C., 2016. Restorations of faulted
464 domes. Am. Assoc. Pet. Geol. Bull. 100, 151–163. doi:10.1306/08171514211
- 465 Ameen, M.S., 2014. Fracture and in-situ stress patterns and impact on performance in
466 the Khuff structural prospects, eastern offshore Saudi Arabia. Mar. Pet. Geol. 50,
467 166–184. doi:10.1016/j.marpetgeo.2013.10.004
- 468 Ameen, M.S., Buhidma, I.M., Rahim, Z., 2010. The function of fractures and in-situ
469 stresses in the Khuff reservoir performance, onshore fields, Saudi Arabia. Am.
470 Assoc. Pet. Geol. Bull. 94, 27–60. doi:10.1306/06160909012
- 471 Amer, A., Chinellato, F., Collins, S., Denichou, J.-M., Dubourg, I., Griffiths, R.,
472 Koepsell, R., Lyngra, S., Marza, P., Roberts, I.B., 2013. Structural Steering — A
473 Path to Productivity. Oilf. Rev. 14–31.
- 474 Barton, N., Bandis, S., Bakhtar, K., 1985. Strength, deformation and conductivity
475 coupling of rock joints. Int. J. Rock Mech. Min. Sci. Geomech. Abstr. 22, 121–
476 140. doi:10.1016/0148-9062(85)93227-9
- 477 Barton, N., Choubey, V., 1977. The shear strength of rock joints in theory and
478 practice. Rock Mech. Felsmechanik Mec. des Roches 10, 1–54.
479 doi:10.1007/BF01261801
- 480 Brown, J., Davis, B., Gawankar, K., Kumar, A., Li, B., Killer, C.K., Laronga, R.,
481 Schlicht, P., 2015. Imaging: Getting the Picture Downhole. Oilf. Rev. 27, 4–21.
- 482 Dershowitz, W.S., Herda, H.H., 1992. Interpretation of fracture spacing and intensity.
483 Dunham, R.J., 1962. Classification of carbonate rocks according to depositional
484 texture, in: M 1: Classification of Carbonate Rocks--A Symposium. p. 23.
- 485 Ekstrom, M.P., Dahan, C.A., Chen, M.Y., Lloyd, P.M., Rossi, D.J., 1987. Geological
486 Formation Imaging With Microelectrical Scanning Arrays, in: The Log Analyst.
487 pp. 294–306.
- 488 Ekstrom, M.P., Dahanl, C.A., Chen, M.-Y., Lloyd, P.M., Rossi, D.J., 1986. Formation
489 imaging with microelectrical scanning arrays, in: SPWLA Twenty-Seventh

- Annual Logging Symposium, June 9-13, 1986. pp. 1–21.
- Heffer, K.J., Lean, J., 1993. Earth stress orientation—a control on, and a guide to, flooding directionality in a majority of reservoirs, in: W. Linville (Ed.), *Reservoir Characterization III*, PennWell Books, Tulsa. pp. 799–822.
- Khoshbakht, F., Azizzadeh, M., Memarian, H., Nourozi, G.H., Moallemi, S.A., 2012. Comparison of electrical image log with core in a fractured carbonate reservoir. *J. Pet. Sci. Eng.* 86–87, 289–296. doi:10.1016/j.petrol.2012.03.007
- Luthi, S.M., Souhaité, P., 1990. Fracture apertures from electrical borehole scans. *Geophysics* 55, 821–833.
- MacPherson, K.A.T., Ameen, M.S., 2014. Fractures in the Jurassic Arab formation and Lower Fadhili carbonate member of the Dhurma Formation, Saudi Arabia, in: *76th EAGE Conference & Exhibition 2014 Amsterdam RAI, The Netherlands*, 16-19 June 2014. pp. 16–19.
- Mitchell, J.C., Lehmann, P.J., Cantrell, D.L., Al-Jallal, I.A., Al-Thagafy, M.A.R., 1988. Lithofacies, Diagenesis and Depositional Sequence; Arab-D Member, Ghawar Field, Saudi Arabia, in: A.J. Lomando and P.M. Harris (Eds.), *Giant Oil and Gas Fields - A Core Workshop*. Society of Economic Paleontologists and Mineralogists, Core Workshop. pp. 459–514.
- Nelson, R.A., 2001. Geologic Analysis of Naturally Fractured Reservoirs, *Geologic Analysis of Naturally Fractured Reservoirs*. doi:10.1016/B978-088415317-7/50005-1
- Ogata, K., Senger, K., Braathen, A., Tveranger, J., Olausson, S., 2014. The importance of natural fractures in a tight reservoir for potential CO₂ storage: a case study of the upper Triassic–middle Jurassic Kapp Toscana Group (Spitsbergen, Arctic Norway). *Geol. Soc. London, Spec. Publ.* 374, 395–415. doi:10.1144/SP374.9
- Ozkaya, S.I., 2008. Using Probabilistic Decision Trees to Detect Fracture Corridors From Dynamic Data in Mature Oil Fields. *SPE Reserv. Eval. Eng.* 11, 1061–1070. doi:10.2118/105015-PA
- Ponziani, M., Slob, E., Luthi, S., Bloemenkamp, R., Le Nir, I., 2015. Experimental validation of fracture aperture determination from borehole electric microresistivity measurements. *GEOPHYSICS* 80, D175–D181. doi:10.1190/geo2014-0334.1
- Pöppelreiter, M., García-Carballido, C., Kraaijveld, M., 2010. Dipmeter and borehole image log technology, *AAPG Memoir* 92.
- Prilliman, J., Bean, C.L., Hashem, M., Bratton, T., Fredette, M.A., Lovell, J.R., 1997. A comparison of wireline and LWD resistivity images in the Gulf of Mexico, in: *SPWLA 38th Annual Logging Symposium*, 15-18 June, Houston, Texas. pp. 1–9.
- Spies, B.R., 1996. Electrical and electromagnetic borehole measurements: A review. *Surv. Geophys.* 17, 517–556. doi:10.1007/BF01901643
- Tehrani, M.A., Sawdon, C.A., Levey, S.J.M., 2002. Electrically conductive oil-based mud. *Proc. Chemistry Oil Ind. VII Meet. held Manchester* 13-14 Nov. 2001, Ed. by T. Balson, H.A. Craddock, J. Dunlop, H. Fram. G. Payne P. Reid, R. Soc. Chemistry 41–46.
- Wang, W.H., Thagafy, M.M., 2017. Applications of High-Resolution LWD Resistivity Image Logs for Carbonate Reservoir Characterization, in: *SPE Kingdom of Saudi Arabia Annual Technical Symposium and Exhibition*. Society of Petroleum Engineers, p. 13. doi:10.2118/188115-MS
- Zhao, J., 1997. Joint surface matching and shear strength Part B: JRC-JMC Shear

Borehole	Borehole deviation	Borehole azimuth	FMI length	FMI in carbonate	FMI in anhydrite	Cored interval	Damaged core	Core recovery factor
	Degrees	Degrees	m	m	m	m	m	(%)
X-01	71	55	481.3	274	207.3	91.4	1.4	98%
X-02	76	42	665.1	495	170.1			
X-03	48	16	271.0	198.1	72.8	189.0	3.6	98%
X-04	70	16	388.3	331.3	57.0			

Table 1: Borehole data coverage of core and borehole images.

Figure captions

Fig. 1. a) The map of the study area in Eastern Arabia, including the regional trend of the S_{Hmax} b) subsurface structural map displaying part of the petroleum field of the dome structure and the locations of the directional boreholes (X-01, X-02, X-03 and X-04), and c) scaled graphs demonstrate the borehole geometry, data types, and data coverage across the Arab carbonate reservoirs (A, B, C, and D). Note: The tops of the imaged intervals coincide with the carbonate reservoir tops in X-04, X-03, and X-01.

Fig. 2. At left, a column of the described rock facies of the Arab reservoirs (A, B, C and D) from the core of X-01 and X-03 boreholes.

Fig. 3. a) Photographs for some examples of the core, a) displaying one side of the core, b) displaying 360° of the whole core exterior, from the industrial scanner, and c) displaying part of the core slabs. The core was photographed in (a) and (b) before the core slabbing, which was done later for geologic lithological descriptions.

Fig. 4. a) The profile of a barren fracture (green arrows) from a core sample and its 360° photograph. The 360° photographs of the core were used to trace and digitize fractures and veins into digital profiles of up to 0.1 mm resolution. b) Typical examples of the digital profiles used for measurements of widths, roughness and wall mismatch. Below are two examples of the profiles we excluded from the measurements due to their geometrical complexity, reflecting short profiles around the core, or damage in the core fracture edge. c) One example of a digital profile displaying how the widths of fractures and veins were estimated, and d) the same profile is separated into top and base traces to show how the roughness and wall mismatches were measured using a fitted smooth curve and several other computational techniques, described in (Al-Fahmi, et al., 2018).

Fig. 5. Examples of barren fractures from a), b) the core and c), d) the borehole images. Barren fractures and calcite veins are mostly parallel (i.e., sets), and steep to the nearly flat bedding and bed-parallel stylolite planes.

Fig. 6. Orientation measurements of open barren fractures from the borehole images for a) dips, b) strikes, c) combined dips and strikes from the four boreholes, d) stereonet (Schmidt pole and plane lower hemisphere) displaying dips and strikes of the veins and barren fractures.

Fig. 7. a) Widths of the described calcite veins and barren fractures from the core, b) apertures of the barren fractures in borehole images plotted against the fracture strikes in (6b). The plot shows a trend from which we observe that apertures of the NE-SW and E-W trending fractures are relatively larger than those of the NW-SE fractures. Also, the plot shows separation between the

1
2
3
4
5
6
7
8
9
10
11
12
13
14
15
16
17
18
19
20
21
22
23
24
25
26
27
28
29
30
31
32
33
34
35
36
37
38
39
40
41
42
43
44
45
46
47
48
49
50
51
52
53
54
55
56
57
58
59
60
61
62
63
64
65

585 mechanical and hydraulic apertures for most of the NW-SE fractures, linking
586 their detected apertures to mismatching walls. Detection levels are included
587 for X-01 (20%) and X-03 (54%). c) 360° photographs of the core exterior
588 displaying variations in fracture widths, ranging from small (0.5 mm) at right to
589 large (5 mm) at left of the core photographs. The photographs also display
590 that the widths depend on the roughness and wall mismatch, which are
591 product of the primary and diagenetic fabrics of the host carbonates (Al-Fahmi
592 et al., 2018). d) Range of roughness and wall mismatch, mostly from the NW-
593 SE fractures. The barren fractures are mostly of matching walls. This
594 observation complements other two observations. The first is that the majority
595 of the NW-SE fractures are missing in boreholes images, especially from X-
596 01. The second is that the detected fractures are mostly of mismatching walls.

597 Fig. 8. A layout for the interpreted and compared fractures and veins from the
598 core and borehole images of X-01 and X-03. The barren fractures are clearly
599 more abundant than the calcite veins in the Arab reservoirs (A, B, C, and D).
600 The borehole images provided limited and inconsistent detections and hence
601 variable abundances for fractures and veins. The borehole images of X-03
602 provided better detection for barren fractures than the borehole images of X-
603 01.

604 Fig. 9. Two examples displaying strong- and weak-resistivity contrast between
605 fractures, veins and host rocks. a) a 360° core photograph of an open and
606 rough fracture that is barely seen as conductive feature from the equivalent
607 borehole images due to the highly porous “conductive” fabrics of the host bed.
608 In (b) calcite veins in the core of 0.5-mm widths that are detected as resistive

1
2
3
4
5
6
7
8
9
10
11
12
13
14
15
16
17
18
19
20
21
22
23
24
25
26
27
28
29
30
31
32
33
34
35
36
37
38
39
40
41
42
43
44
45
46
47
48
49
50
51
52
53
54
55
56
57
58
59
60
61
62
63
64
65

609 features in the borehole images, apparently due to the contrast between the
610 resistive signature and the porous (and hence conductive) fabrics of the host
611 bed.

612 Fig. 10. Different signatures (traces) for the barren open fractures in borehole
613 images; a, b) the LWD images of X-02, c) wireline images of X-01, and d)
614 wireline images of X-03. The fracture apertures in (b) were notably large, most
615 likely due to strong infiltrations of the high-pressure drilling fluid into these
616 fractures.

617 Fig. 11. a) An idealized model demonstrating (open) aligned and (closed) non-
618 aligned barren fractures in Eastern Arabia. Fracture apertures depend on the
619 present-day S_{Hmax} and the mismatching walls preventing complete fracture
620 closure under the S_{Hmax} . b) factors governing, or influencing, the fracture
621 detection by modern borehole imagers (FMI HD) in carbonate reservoirs.
622 Fractures are detected if they have relatively larger widths, more than ~2 mm.
623 Widths of fracture apertures are dependent on the stress field (opening and
624 closing stresses), and degree of wall-roughness mismatching. Fractures with
625 matching walls can be closed completely making the apertures undetected in
626 borehole images, but wall mismatch preserves apertures under the fracture
627 closure. Other influencing factors include resistivity contrast improving, or
628 reducing, signatures of fractures against their host (background) rocks, and
629 aperture fluid intake according to the balance of the fluid pressure between
630 borehole conductive mud and reservoir non-conductive oil and gas.

Fig. 1

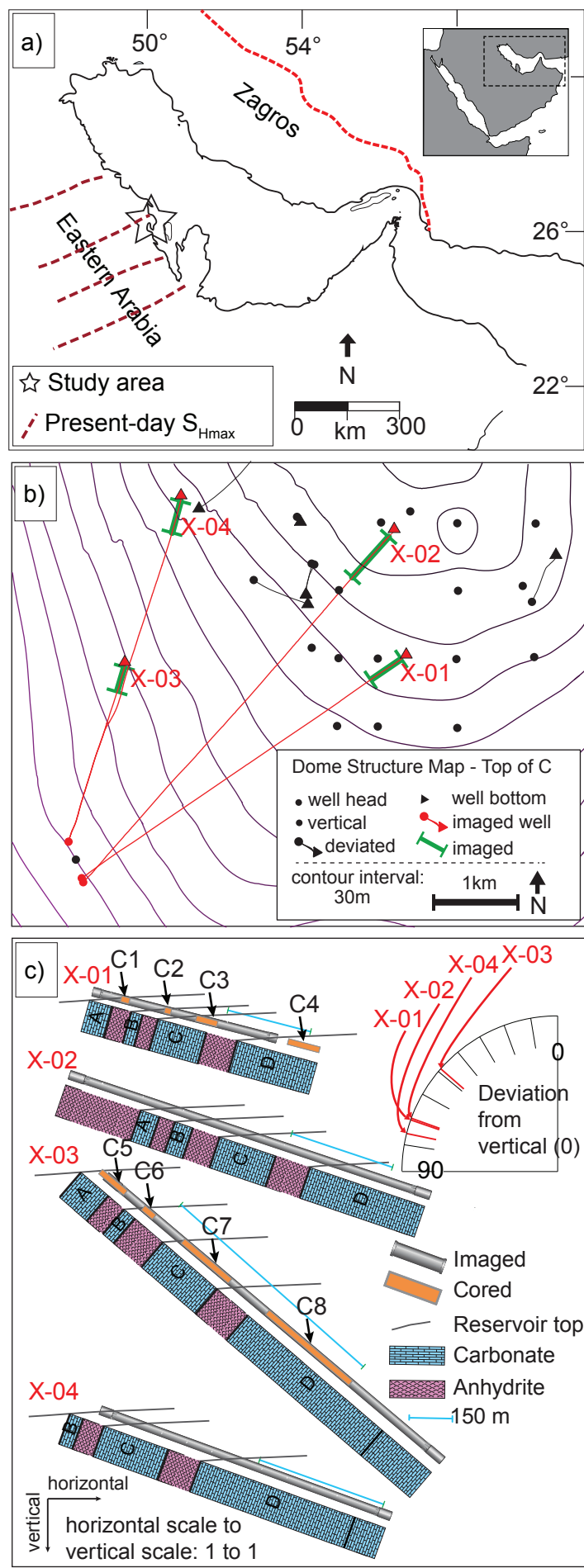


Fig. 2

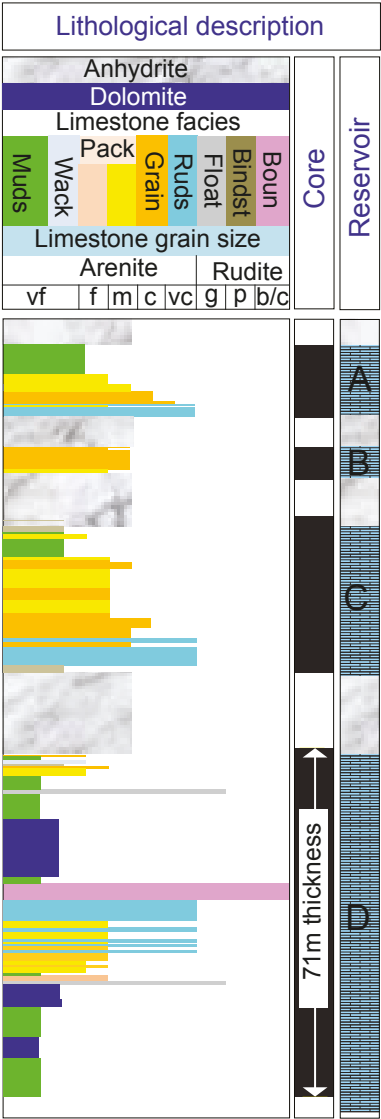


Fig. 3

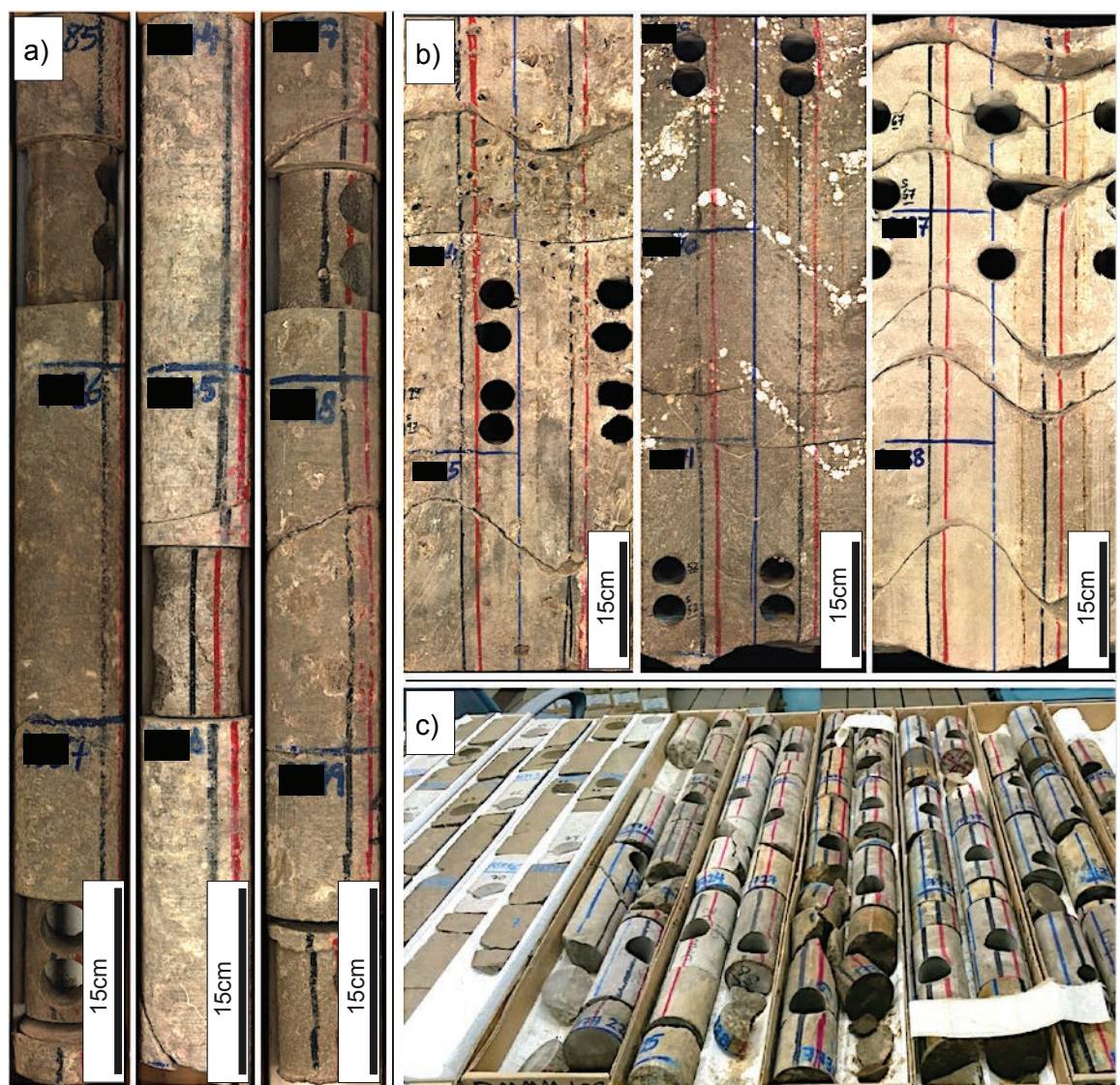


Fig. 4

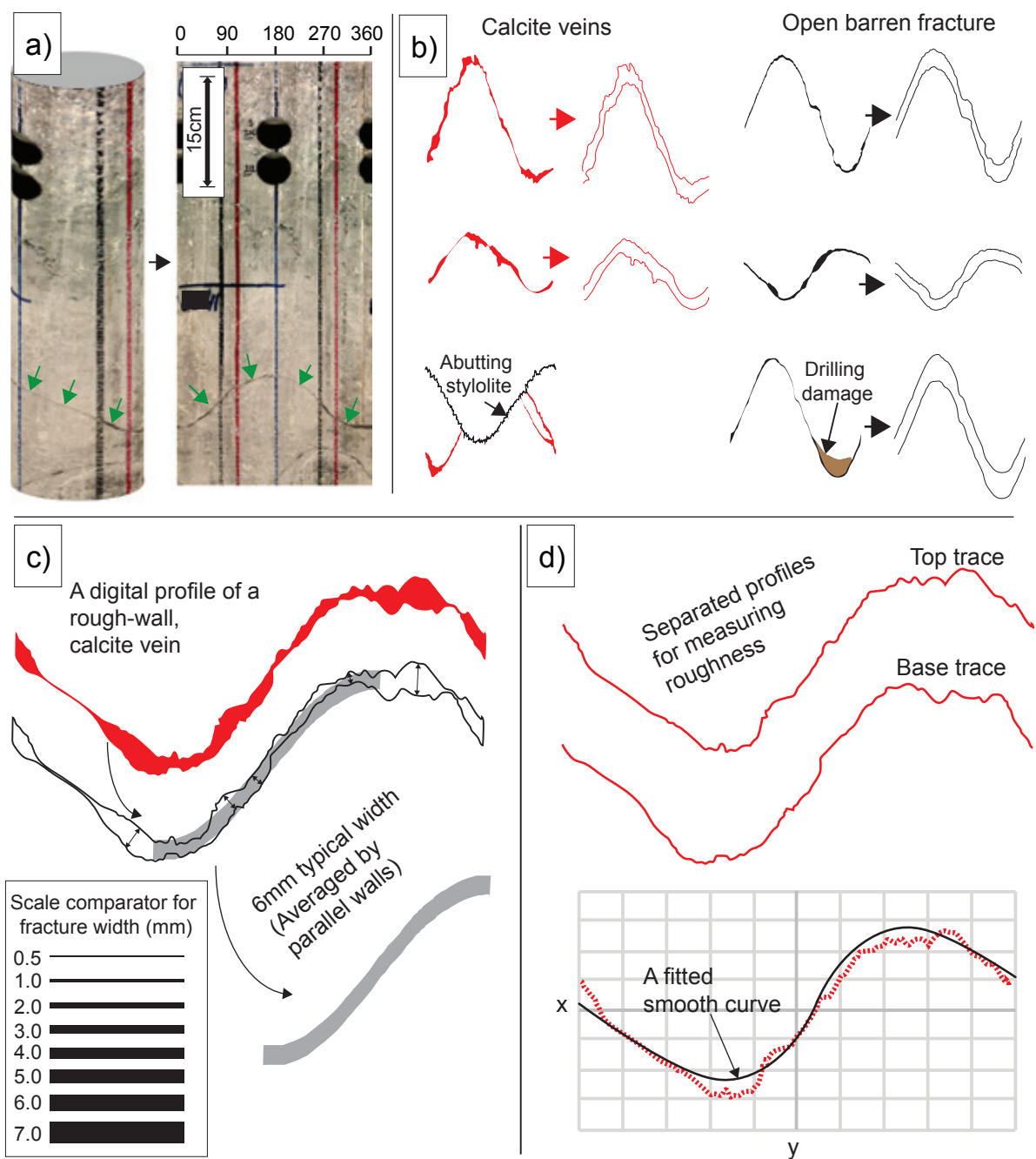


Fig. 5

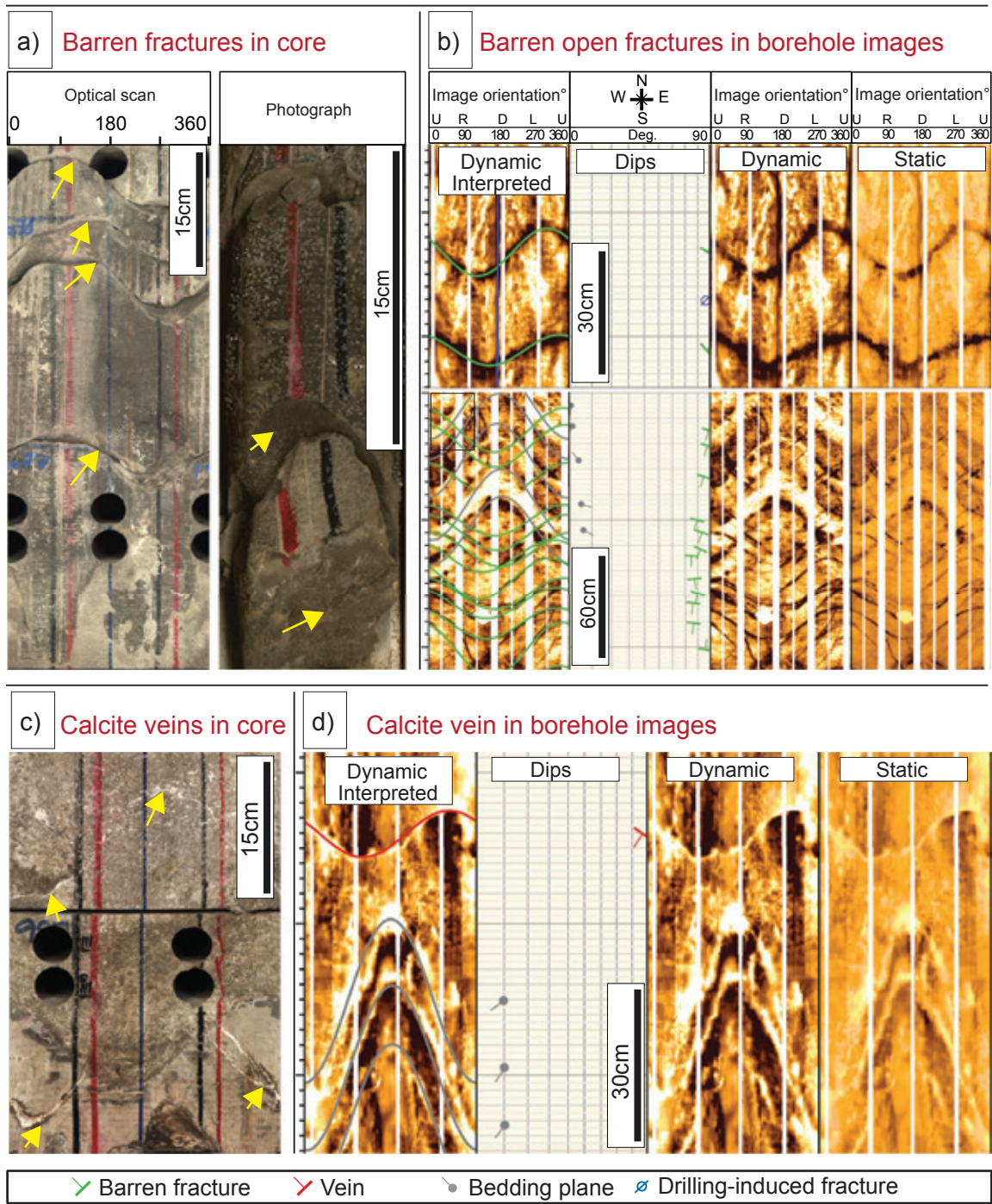


Fig. 6

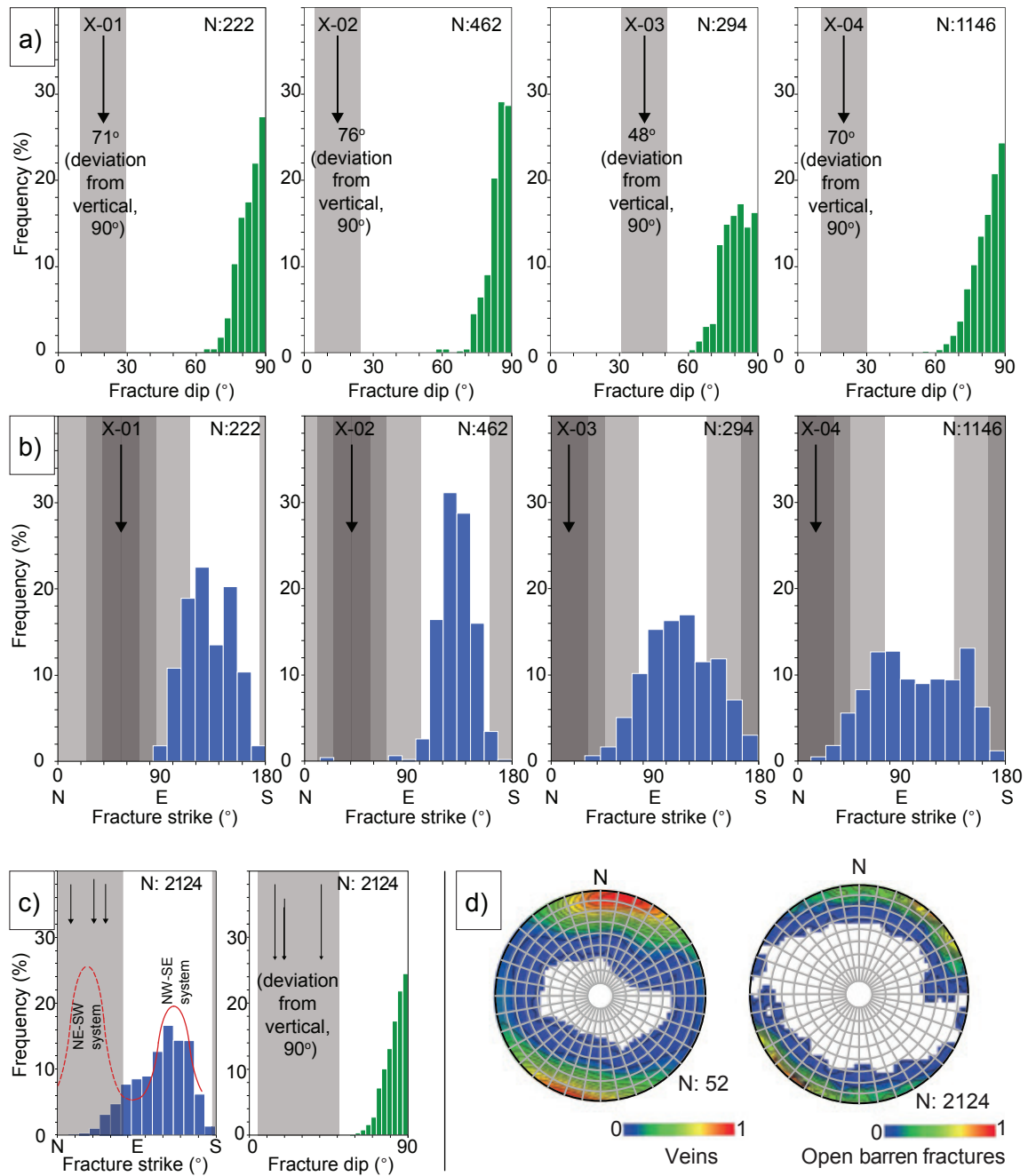


Fig. 7

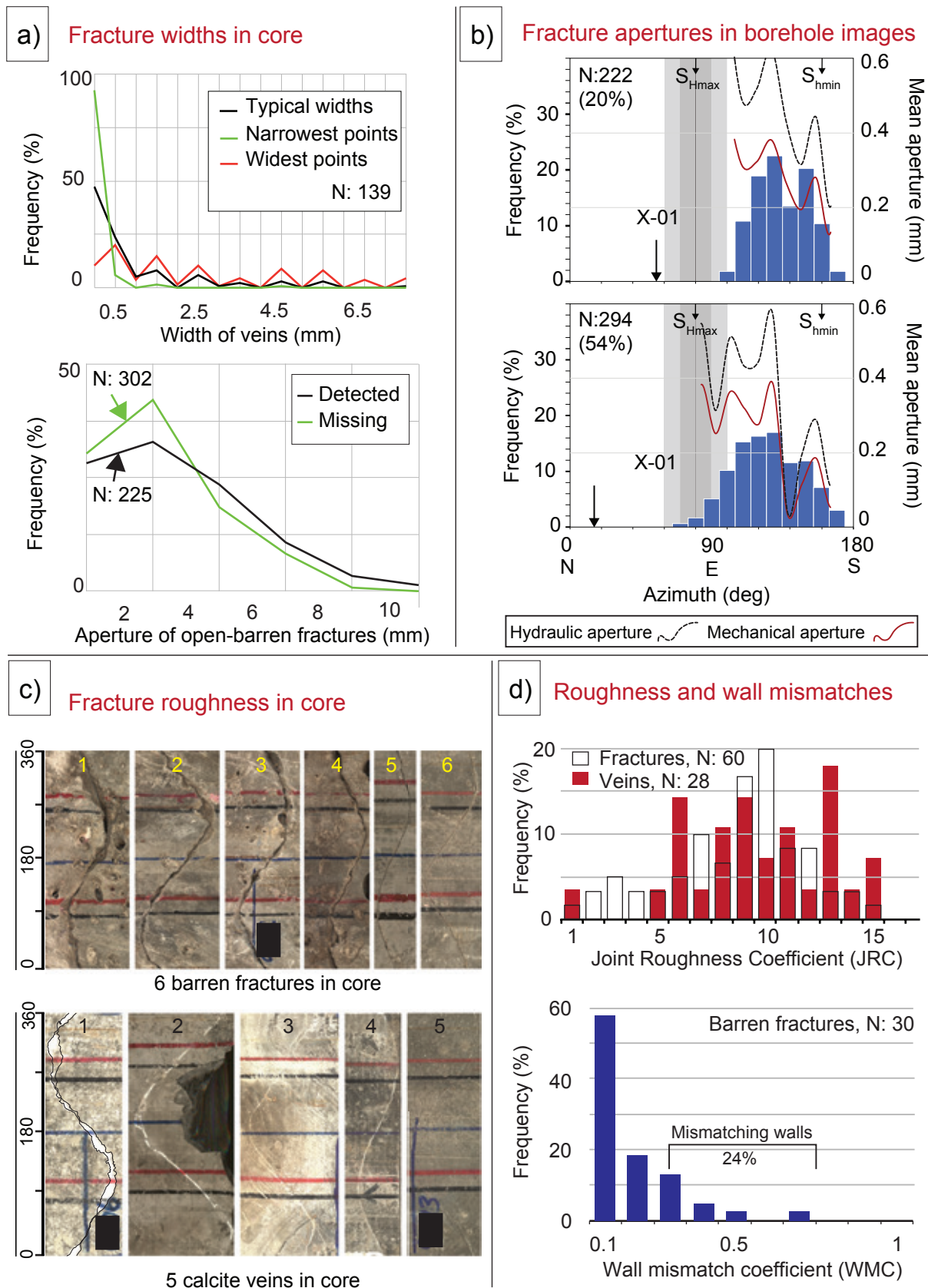


Fig. 8

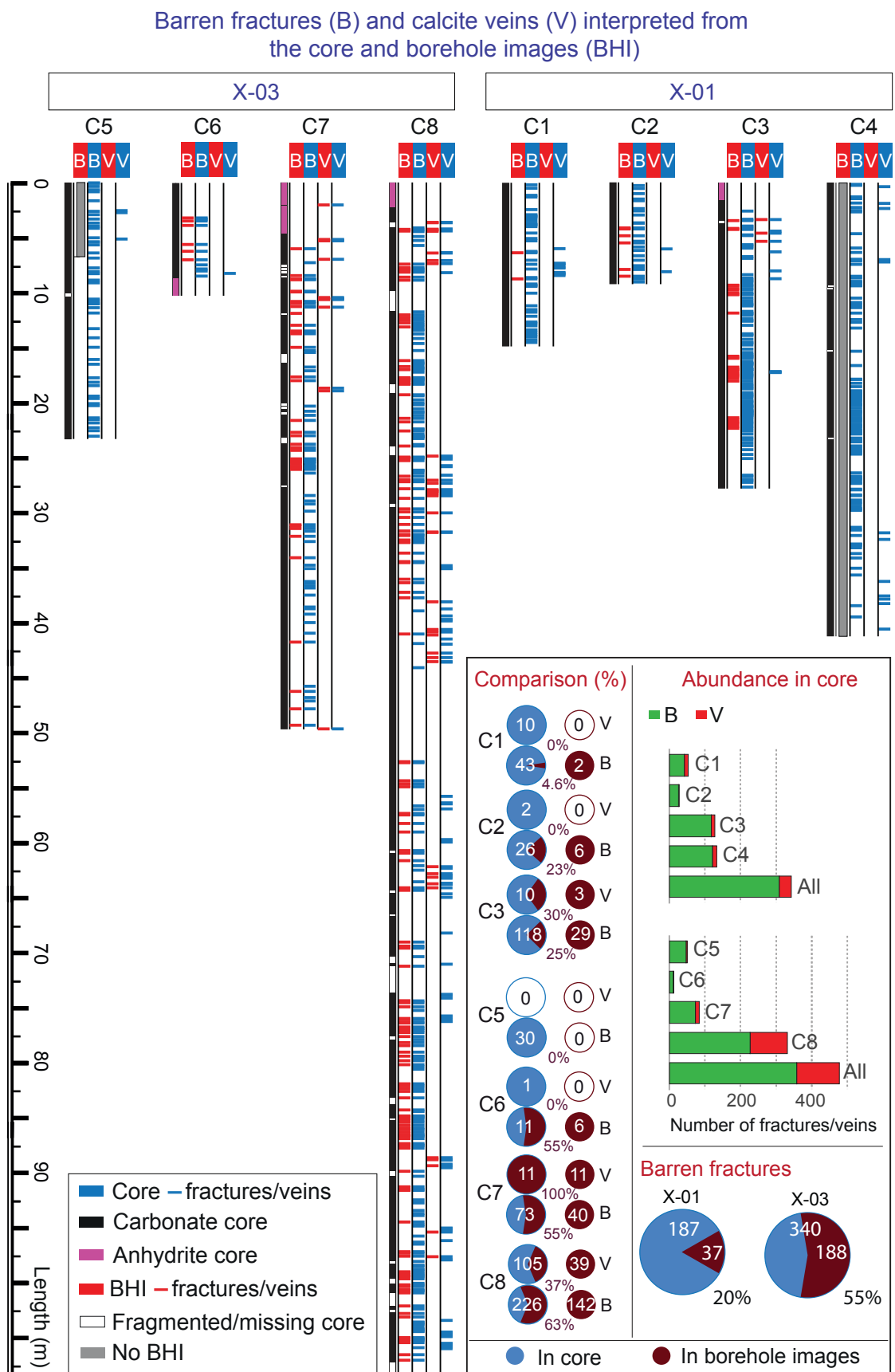


Fig. 9

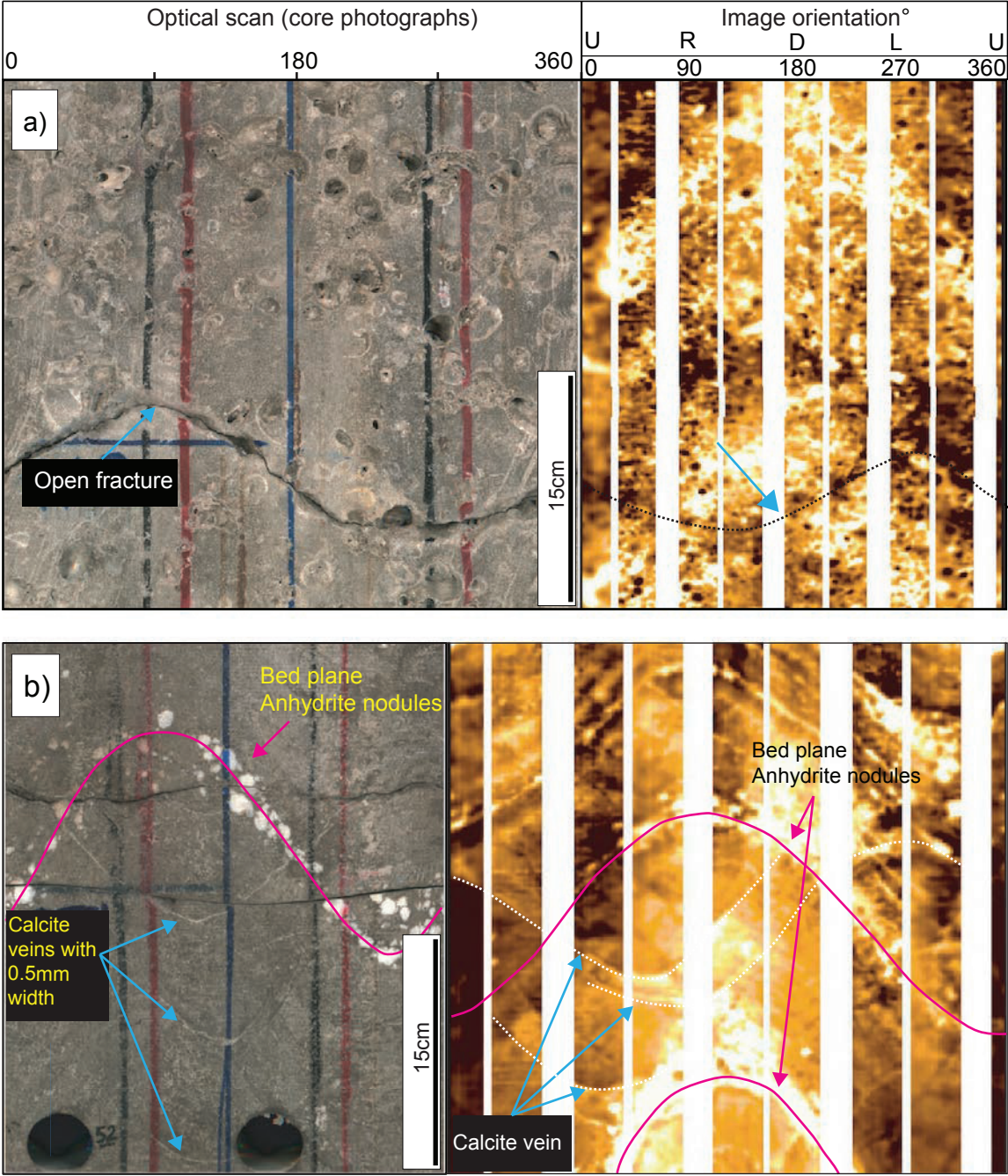


Fig. 10

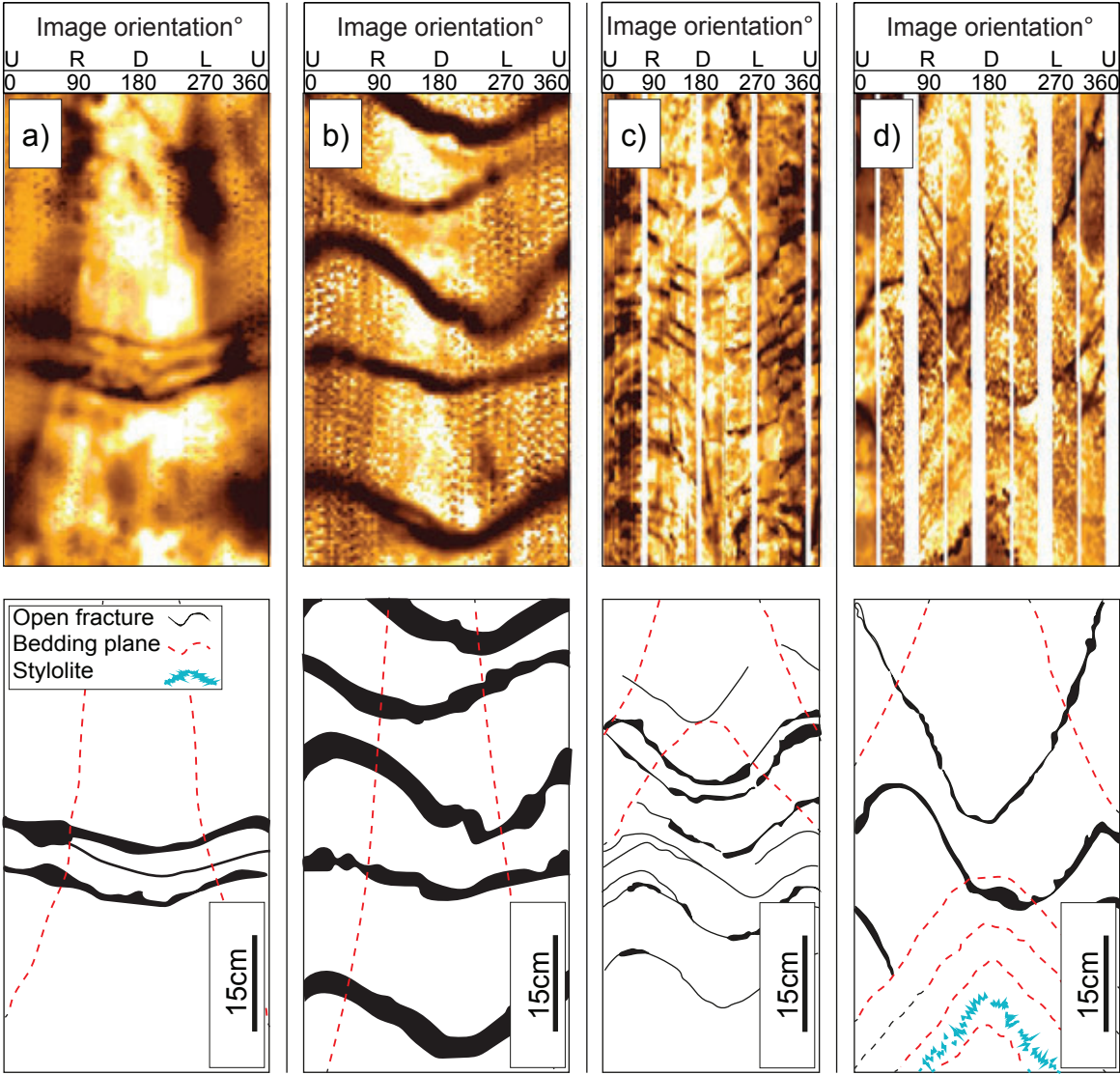


Fig. 11

